

Three-body physics under dissipative spin-orbit coupling

Xi Zhao(赵茜)†

Citation: Chin. Phys. B, 2025, 34 (**3**): 033101. DOI: 10.1088/1674-1056/ada43e
Journal homepage: http://cpb.iphy.ac.cn; http://iopscience.iop.org/cpb

What follows is a list of articles you may be interested in

All-electron basis sets for H to Xe specific for ZORA calculations: Applications in atoms and molecules

C. S. Gomes, F. E. Jorge, and A. Canal Neto
Chin. Phys. B, 2024, 33 (**8**): 083101. DOI: 10.1088/1674-1056/ad4bbe

Low-lying electronic states of osmium monoxide OsO

Wen Yan(严汶) and Wenli Zou(邹文利)
Chin. Phys. B, 2023, 32 (**11**): 113101. DOI: 10.1088/1674-1056/acec46

Highly accurate theoretical study on spectroscopic properties of SH including spin-orbit coupling

Shu-Tao Zhao(赵书涛), Xin-Peng Liu(刘鑫鹏), Rui Li(李瑞), Hui-Jie Guo(国慧杰), and Bing Yan(闫冰)
Chin. Phys. B, 2021, 30 (**7**): 073104. DOI: 10.1088/1674-1056/ac003f

Configuration interaction study on low-lying states of AlCl molecule

Xiao-Ying Ren(任笑影), Zhi-Yu Xiao(肖志宇), Yong Liu(刘勇), and Bing Yan(闫冰)
Chin. Phys. B, 2021, 30 (**5**): 053101. DOI: 10.1088/1674-1056/abd46a

Vibronic spectra of aluminium monochloride relevant to circumstellar molecule

Jian-Gang Xu(徐建刚), Cong-Ying Zhang(张聪颖), Yun-Guang Zhang(张云光)
Chin. Phys. B, 2020, 29 (**3**): 033102. DOI: 10.1088/1674-1056/ab6c46

Three-body physics under dissipative spin–orbit coupling

Xi Zhao(赵茜)[†]

CAS Key Laboratory of Quantum Information, University of Science and Technology of China, Hefei 230026, *China*

(Received 13 December 2024; accepted manuscript online 31 December 2024)

We study the trimer state in a three-body system, where two of the atoms are subject to Rashba-type spin–orbit coupling and spin-dependent loss while interacting spin-selectively with the third atom. The short-time conditional dynamics of the three-body system is effectively governed by a non-Hermitian Hamiltonian with an imaginary Zeeman field. Remarkably, the interplay of non-Hermitian single particle dispersion and the spin-selective interaction results in a Borromean state and an enlarged trimer phase. The stability of trimer state can be reflected by the imaginary part of trimer energy and the momentum distribution of trimer wave function. We also show the phase diagram of the three-body system under both real and imaginary Zeeman fields. Our results illustrate the interesting consequence of non-Hermitian spectral symmetry on the few-body level, which may be readily observable in current cold-atom experiments.

Keywords: few-body physics, non-Hermitian physics, spin–orbit coupling, Borromean state

PACS: 31.15.ac, 21.45.–v, 64.70.–p, 67.85.–d

DOI: 10.1088/1674-1056/ada43e **CSTR:** 32038.14.CPB.ada43e

1. Introduction

Open quantum systems exhibit remarkably different properties from their closed counterparts and are essential for understanding quantum systems in realistic environments.[1–3] An effective non-Hermitian description is often employed to characterize these systems, particularly for capturing the short-time conditional dynamics where quantum jumps are absent.[1,4] A significant feature of non-Hermitian Hamiltonians is the possibility of hosting spectral singularities, known as exceptional points.[5–7] At these exceptional points, eigenvectors and eigenvalues coalesce, giving rise to unique dynamical and topological phenomena, which have potential applications in areas such as sensing and non-reciprocal transport.[8–13] Many of these properties have been demonstrated in open quantum systems that are typically non-interacting or single-particle systems, where non-Hermitian Hamiltonians naturally emerge under post-selection conditions.[14–20] For instance, non-Hermiticity can be realized in cold atom experiments through laser-induced one-body[19,20] or two-body[21–24] dissipation. As a result, the particle-number or internal-spin dynamics in these systems are governed by PT-symmetric non-Hermitian Hamiltonians. In this context, given the flexible control of interactions in quantum gases, it is highly desirable to gain a deeper understanding of the effects of interactions in non-Hermitian systems. This contrasts with previous studies on few- or many-body phenomena in open systems driven by the full Lindblad master equation, which primarily focus on steady-state properties in long-time unconditional dynamics.[25,26]

Few-body system serves as a starting point for studying interacting non-Hermitian systems. On one hand, few-body systems are the fundamental building blocks of many-body phenomena and are more easily realized in experiments.[27–31] On the other hand, existing studies on non-Hermitian few-body physics have revealed that non-Hermiticity can lead to novel few-body phenomena, such as the enhancement of dimer formation, the emergence of super-stable dimer states, and the Efimov physics.[29,37,38]

In this work, we study a two-component Fermi atom (denoted as a) subject to Rashba spin–orbit coupling (SOC) and Zeeman field, while interacting with a free atom (denoted as b), as shown in Fig. 1(a). In this context, an imaginary Zeeman field can be interpreted as spin-selective atom loss, a phenomenon recently demonstrated in several experiments.[19,20] The single-particle dispersion spectrum of the two-component system under Rashba SOC alone forms a degenerate ring in momentum space, referred to as the Rashba ring.[33] In the presence of an additional imaginary Zeeman field, an exceptional ring emerges. Previous studies have shown that the spectral symmetry of the Rashba SOC dispersion plays a crucial role in the formation of few-body states.[34,35] Here we show that a trimer bound state, particularly a Borromean state, as schematically shown in Fig. 1(b), in which any subsystem of its two components is unbound, can emerge in a dissipative spin–orbit coupling system. Here we focus on the physics of three-body state under this non-Hermitian setting. We find that the single-particle dissipation deepens the strength of a trimer bound energy, which is much deeper than the strength of the dimer bound energy, leading to an enlarged region for the existence of the trimer phase.

[†]Corresponding author. E-mail: zx4612@mail.ustc.edu.cn

© 2025 Chinese Physical Society and IOP Publishing Ltd. All rights, including for text and data mining, AI training, and similar technologies, are reserved.

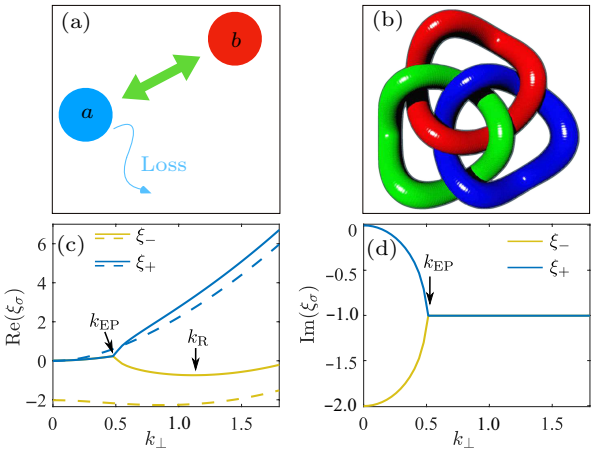


Fig. 1. (a) A schematic diagram of the interaction between dissipative atom a and atom b. (b) A schematic diagram of a Borromean ring, where removing any one of the three rings causes the remaining two rings to decouple. (c) Real parts of the single-particle spectra under Rashba SOC in the presence of a real (dashed lines) or imaginary (solid lines) Zeeman field. (d) Imaginary parts of the single-particle spectra under Rashba SOC with an imaginary Zeeman field. Here, $k_{\rm EP}$ and $k_{\rm R}$ denote the radius of the exceptional ring and the location of the energy minimum, respectively. In panels (c) and (d), $k_z = 0$ is considered, and the real or imaginary Zeeman field has the same magnitude, $|B| = E_0$. In all plots, the units of momentum and energy are λ and $E_0 = \lambda^2/(2m_a)$, respectively.

The rest parts of this paper are organized as follows. In Section 2, we set up the basic model of the non-Hermitian system and study the single-particle properties. We then study the trimer state and phase diagram in Sections 3 and 4, respectively.

2. Model and single-particle properties

We consider a three-body problem, where the internal spin states of one Fermi atom species a are coupled through a Rashba-type SOC. One of the spin states, say the spin-down component ($|\downarrow\rangle$), is also subject to a Zeeman field which can be either real or imaginary, depending on its physical origin. Specifically, the Zeeman field is real under a spin-selective light shift or external magnetic field; it is imaginary when representing laser-induced loss. We then consider an s-wave interatomic interaction between the spin-up component of a species and the second atom species b. The non-Hermitian effective Hamiltonian of this system is (we take $\hbar = 1$ throughout the work)

$$\begin{aligned} H =& \sum_{\boldsymbol{k},\sigma=\uparrow,\downarrow} \varepsilon^a_{\boldsymbol{k}} a^\dagger_{\boldsymbol{k},\sigma} a_{\boldsymbol{k},\sigma} + \sum_{\boldsymbol{k}} \varepsilon^b_{\boldsymbol{k}} b^\dagger_{\boldsymbol{k}} b_{\boldsymbol{k}} \\ &+ \frac{\lambda}{m_a} \sum_{\boldsymbol{k}} \left[(k_x - \mathrm{i}k_y)\, a^\dagger_{\boldsymbol{k},\uparrow} a_{\boldsymbol{k},\downarrow} + \mathrm{H.c.} \right] \\ &- 2B \sum_{\boldsymbol{k}} a^\dagger_{\boldsymbol{k},\downarrow} a_{\boldsymbol{k},\downarrow} + \frac{U}{V} \sum_{\boldsymbol{k},\boldsymbol{k}',\boldsymbol{q}} a^\dagger_{\boldsymbol{k},\uparrow} b^\dagger_{\boldsymbol{q}-\boldsymbol{k}} b_{\boldsymbol{q}-\boldsymbol{k}'} a_{\boldsymbol{k}',\uparrow}, \end{aligned} \tag{1}$$

where the operators $a_{\boldsymbol{k},\sigma}$ ($\sigma = \uparrow,\downarrow$) and $b_{\boldsymbol{k}}$ represent the annihilation of two different types of atoms, where $\boldsymbol{k}$ denotes the atomic momentum. The kinetic energies of the atoms are given by $\varepsilon^a_{\boldsymbol{k}} = \boldsymbol{k}^2/(2m_a)$ and $\varepsilon^b_{\boldsymbol{k}} = \boldsymbol{k}^2/(2m_b)$, with m_a and m_b being the respective atomic masses. The parameter λ characterizes the strength of the Rashba SOC, and B is the effective Zeeman field strength, which can be either real or imaginary, corresponding to a real or imaginary magnetic field. The bare interaction strength between the atoms, denoted by U, is related to the s-wave scattering length $a_{\rm s}$ through the renormalization equation $1/U = m_a/(2\pi(1+\eta)a_{\rm s}) - (1/V)\sum_{\boldsymbol{k}} 1/(1+\eta)\varepsilon^a_{\boldsymbol{k}}$, where V is the quantization volume and $\eta = m_a/m_b$ is the mass ratio. The single-particle Hamiltonian of atoms with Rashba SOC and dissipation can be expressed in momentum space as

$$H^a_0(\boldsymbol{k}) = \varepsilon^a_{\boldsymbol{k}}\sigma_0 + \frac{\lambda}{m_a}(k_x\sigma_x + k_y\sigma_y) + B\sigma_z - B\sigma_0, \tag{2}$$

where σ_i ($i = x, y, z$) are the Pauli matrices, and σ_0 is the 2×2 identity matrix. To facilitate later discussions, we transform the annihilation (creation) operators into biorthogonal field operators in the helicity branches:

$$\begin{pmatrix} a^{\mathrm{R}\dagger}_{\boldsymbol{k},+} \\ a^{\mathrm{R}\dagger}_{\boldsymbol{k},-} \end{pmatrix} = U^{\mathrm{T}}_{\boldsymbol{k}} \begin{pmatrix} a^\dagger_{\boldsymbol{k},\uparrow} \\ a^\dagger_{\boldsymbol{k},\downarrow} \end{pmatrix}, \tag{3}$$

$$\begin{pmatrix} a^{\mathrm{L}}_{\boldsymbol{k},+} \\ a^{\mathrm{L}}_{\boldsymbol{k},-} \end{pmatrix} = U^{-1}_{\boldsymbol{k}} \begin{pmatrix} a_{\boldsymbol{k},\uparrow} \\ a_{\boldsymbol{k},\downarrow} \end{pmatrix}, \tag{4}$$

where $\pm$ represents the helicity index. The matrix $U_{\boldsymbol{k}}$ is given by

$$U_{\boldsymbol{k}} = \begin{pmatrix} \gamma^\uparrow_{\boldsymbol{k},+} & \gamma^\uparrow_{\boldsymbol{k},-} \\ \gamma^\downarrow_{\boldsymbol{k},+} & \gamma^\downarrow_{\boldsymbol{k},-} \end{pmatrix}, \tag{5}$$

with the elements defined as

$$\gamma^\downarrow_{\boldsymbol{k},\pm} = \frac{\mathrm{e}^{\mathrm{i}\phi_{\boldsymbol{k}}/2}}{\sqrt{1+|c_{\boldsymbol{k},\pm}|^2}}, \quad \gamma^\uparrow_{\boldsymbol{k},\pm} = \frac{c_{\boldsymbol{k},\pm}\,\mathrm{e}^{\mathrm{i}\phi_{\boldsymbol{k}}/2}}{\sqrt{1+|c_{\boldsymbol{k},\pm}|^2}}, \tag{6}$$

where $c_{\boldsymbol{k},\pm} = \frac{m_a B \pm \sqrt{m_a^2 B^2 + k_\perp^2 \lambda^2}}{\lambda k_\perp}$, $k_\perp = \sqrt{k_x^2 + k_y^2}$, and $\phi_{\boldsymbol{k}} = \arg(k_x, k_y)$. The single-particle dispersions in the two helicity branches are

$$\xi_{\boldsymbol{k},\pm} = \varepsilon^a_{\boldsymbol{k}} \pm \sqrt{\left(\frac{\lambda}{m_a}\right)^2 k_\perp^2 + B^2} - B. \tag{7}$$

We observe significant differences in the single-particle spectra under real and imaginary Zeeman fields. As shown in Figs. 1(c) and 1(d), in the case of a real Zeeman field, the energy remains real and a gap opens at $k_\perp = 0$. However, when the Zeeman field is imaginary, an exceptional ring emerges at $k_{\rm EP} = \lambda|B|/(2E_0)$, with $E_0 = \lambda^2/(2m_a)$. The radius of this exceptional ring increases linearly with the field strength, and at this point, the energy levels and eigenstates coalesce. For $k_\perp < k_{\rm EP}$, the energies become complex. Additionally, a degenerate ring forms in the x–y momentum plane at the local minimum of the lower helicity branch, $\xi_{\boldsymbol{k},-}$, located at $k_{\rm R} = \mathrm{Re}(\lambda\sqrt{1 - B^2/4E_0^2})$, which we refer to as Rashba ring. Unlike the exceptional ring, the radius of the Rashba ring changes

non-monotonically with the Zeeman field. Both the exceptional ring and the Rashba ring play important roles in various few- and many-body phenomena, as previously shown.[34,37]

In particular, under the imaginary Zeeman field, the alignment of the molecular state's wave function along the exceptional ring k_{R} results in a super-stable dimer state. Moreover, the Rashba ring has been shown to facilitate the formation of exotic Borromean states within a Hermitian system.[34] The Rashba ring persists under finite Zeeman fields, whether real or imaginary, and the radius of the exceptional ring varies with the strength of the imaginary Zeeman field, suggesting significant effects on three-body bound states. As we will show later, the imaginary Zeeman field has a profound influence on the properties of the trimer state.

3. Dimer and trimer states

Now we come to the two- and three-body problems. Under the biorthogonal field operators, the Hamiltonian in Eq. (1) becomes

$$\begin{aligned} H =& \sum_{\boldsymbol{k},\beta=\pm} \xi_{\boldsymbol{k},\beta} a^{\mathrm{R}\dagger}_{\boldsymbol{k},\beta} a^{\mathrm{L}}_{\boldsymbol{k},\beta} + \sum_{\boldsymbol{k}} \varepsilon^{b}_{\boldsymbol{k}} b^{\dagger}_{\boldsymbol{k}} b_{\boldsymbol{k}} \\ &+ \frac{U}{V} \sum_{\boldsymbol{k}\boldsymbol{k}'\boldsymbol{q}} \sum_{\beta,\beta'=\pm} R_{\boldsymbol{k},\beta} L_{\boldsymbol{k}',\beta'} a^{\mathrm{R}\dagger}_{\boldsymbol{k},\beta} b^{\dagger}_{\boldsymbol{q}-\boldsymbol{k}} b_{\boldsymbol{q}-\boldsymbol{k}'} a^{\mathrm{L}}_{\boldsymbol{k}',\beta'}, \quad (8) \end{aligned}$$

where $R_{\boldsymbol{k},\pm} = \pm\gamma^{\downarrow}_{\boldsymbol{k},\mp}/\mathrm{Det}\,(U_{\boldsymbol{k}})$ and $L_{\boldsymbol{k},\pm} = \gamma^{\uparrow}_{\boldsymbol{k},\pm}$.

To determine the dimer state, we use the wave function for the two-body bound state given by

$$\left|\psi^{\mathrm{R,L}}_{\mathrm{M}}\right\rangle = \sum_{\boldsymbol{k},\beta=\pm} \psi^{\mathrm{R,L}}_{\beta}(\boldsymbol{k}) b^{\dagger}_{\boldsymbol{Q}-\boldsymbol{k}} a^{\mathrm{R}\dagger}_{\boldsymbol{k},\beta}|0\rangle, \quad (9)$$

where the superscript R and L denotes the right and left eigenstates of the molecule. The molecular state satisfies the eigenvalue equations $H\left|\psi^{\mathrm{R}}_{\mathrm{M}}\right\rangle = E_2\left|\psi^{\mathrm{R}}_{\mathrm{M}}\right\rangle$ and $H^{\dagger}\left|\psi^{\mathrm{L}}_{\mathrm{M}}\right\rangle = E^{*}_2\left|\psi^{\mathrm{L}}_{\mathrm{M}}\right\rangle$, with E_2 representing the energy of the dimer. Here, $\boldsymbol{Q}$ is the center-of-mass momentum of the molecule, $\psi^{\mathrm{R/L}}_{\beta}(\boldsymbol{k})$ are the variational coefficients, and $|0\rangle$ is the vacuum state.

By minimizing the energy functional $\left\langle\psi^{\mathrm{L}}_{\mathrm{M}}\right| H - E_2\left|\psi^{\mathrm{R}}_{\mathrm{M}}\right\rangle$, we derive the following self-consistent equation for the dimer energy E_2:

$$\frac{1}{U} = \frac{1}{V}\sum_{\boldsymbol{k},\beta=\pm} \frac{L_{\boldsymbol{k},\beta} R_{\boldsymbol{k},\beta}}{E_2 - \xi_{\boldsymbol{k},\beta} - \varepsilon^{b}_{\boldsymbol{Q}-\boldsymbol{k}}}. \quad (10)$$

The dimer binding energy is given by $E_{\mathrm{b}} = E_2 - E_{\mathrm{th}}$, where the scattering threshold is $E_{\mathrm{th}} = \min\left[\mathrm{Re}(\xi_{\boldsymbol{k},-})\right]$.

Now, let us consider a system with two particles of type a and one particle of type b, and express the three-body wave function as

$$|\psi^{(3)}_{\mathrm{R}}\rangle = \sum_{\boldsymbol{k},\sigma}\sum_{\boldsymbol{q},\Gamma} \psi^{(3)}_{\mathrm{R}}(-\boldsymbol{k}-\boldsymbol{q};\boldsymbol{k}\sigma;\boldsymbol{q}\Gamma) b^{\dagger}_{-\boldsymbol{k}-\boldsymbol{q}} a^{\mathrm{R}\dagger}_{\boldsymbol{k}\sigma} a^{\mathrm{R}\dagger}_{\boldsymbol{q}\Gamma}|0\rangle, \quad (11)$$

where the wave function coefficient $\psi^{(3)}_{\mathrm{R}}(-\boldsymbol{k}-\boldsymbol{q};\boldsymbol{k}\sigma;\boldsymbol{q}\Gamma)$ satisfies the Schrodinger equation $H|\psi^{(3)}_{\mathrm{R}}\rangle = E_3|\psi^{(3)}_{\mathrm{R}}\rangle$. Here, σ and Γ denote the helicity branch, and $E_3 = E_{3\mathrm{b}} + 2E_{\mathrm{th}}$ represents the total three-body energy, where $E_{3\mathrm{b}}$ is the three-body binding energy. By solving the Schrodinger equation, we obtain the following equation:

$$\begin{aligned} &\psi^{(3)}_{\mathrm{R}}(-\boldsymbol{k}-\boldsymbol{q};\boldsymbol{k}\sigma;\boldsymbol{q}\Gamma) \\ =& \frac{1}{E_3 - \varepsilon^{b}_{\boldsymbol{k}+\boldsymbol{q}} - \xi_{\boldsymbol{k},\sigma} - \xi_{\boldsymbol{q},\Gamma}} \\ &\times \left(\frac{U}{V}\sum_{\boldsymbol{k}',\sigma'} \psi^{(3)}_{\mathrm{R}}(-\boldsymbol{k}'-\boldsymbol{q};\boldsymbol{k}'\sigma';\boldsymbol{q}\Gamma) R_{\boldsymbol{k},\sigma} L_{\boldsymbol{k}',\sigma'} \right. \\ &\left. - \frac{U}{V}\sum_{\boldsymbol{q}',\Gamma'} \psi^{(3)}_{\mathrm{R}}(-\boldsymbol{k}-\boldsymbol{q}';\boldsymbol{k}\sigma;\boldsymbol{q}'\Gamma') R_{\boldsymbol{q},\Gamma} L_{\boldsymbol{q}',\Gamma'} \right). \quad (12) \end{aligned}$$

By defining an auxiliary function

$$F_{\sigma}(\boldsymbol{k}) = U\sum_{\boldsymbol{q}\Gamma} \psi^{(3)}_{\mathrm{R}}(-\boldsymbol{k}-\boldsymbol{q};\boldsymbol{k}\sigma;\boldsymbol{q}\Gamma) L_{\boldsymbol{k}\sigma} L_{\boldsymbol{q}\Gamma},$$

we derive the equation

$$\frac{1}{U}F_{\sigma}(\boldsymbol{k}) = \frac{1}{V}\sum_{\boldsymbol{q},\Gamma} \frac{F_{\sigma}(\boldsymbol{k}) R_{\boldsymbol{q}\Gamma} L_{\boldsymbol{q}\Gamma} - F_{\Gamma}(\boldsymbol{q}) R_{\boldsymbol{k},\sigma} L_{\boldsymbol{k},\sigma}}{E_3 - \varepsilon^{b}_{\boldsymbol{k}+\boldsymbol{q}} - \xi_{\boldsymbol{k},\sigma} - \xi_{\boldsymbol{q},\Gamma}}. \quad (13)$$

For a system with rotational symmetry about the z-axis, we can decompose the auxiliary function $F_{\sigma}(\boldsymbol{k})$ into different angular momentum sectors:

$$F_{\sigma}(\boldsymbol{k}) = \sum F^{(n)}_{\sigma}(k_{\perp},k_z)\cos(n\phi_{\boldsymbol{k}} + \theta_n), \quad (14)$$

where θ_n is an arbitrary phase shift independent of the binding energy solution. For the ground state, due to Fermi statistics, only the $n = 1$ angular momentum sector needs to be retained, giving the equation

$$\begin{aligned} &\left(\frac{1}{U} - \frac{1}{V}\sum_{\boldsymbol{q}\Gamma} \frac{R_{\boldsymbol{q}\Gamma} L_{\boldsymbol{q}\Gamma}}{E_3 - \varepsilon^{b}_{\boldsymbol{k}+\boldsymbol{q}} - \xi_{\boldsymbol{k},\sigma} - \xi_{\boldsymbol{q},\Gamma}}\right) F_{\sigma}(\boldsymbol{k}) \\ =& -\frac{1}{V}\sum_{\boldsymbol{q},\Gamma} \frac{R_{\boldsymbol{k},\sigma} L_{\boldsymbol{k},\sigma} F_{\Gamma}(\boldsymbol{q})}{E_3 - \varepsilon^{b}_{\boldsymbol{k}+\boldsymbol{q}} - \xi_{\boldsymbol{k},\sigma} - \xi_{\boldsymbol{q},\Gamma}}. \quad (15) \end{aligned}$$

Using the integral identity $\int_0^{2\pi}\cos(mx)\cos(nx)\,\mathrm{d}x = \pi\delta_{m,n}$, we can multiply both sides of the equation by the cosine function and integrate, resulting in a solvable equation

$$\begin{aligned} &\left(\frac{1}{U} - \frac{1}{V}\sum_{\boldsymbol{q}\Gamma} \frac{R_{\boldsymbol{q}\Gamma} L_{\boldsymbol{q}\Gamma}}{E_3 - \varepsilon^{b}_{\boldsymbol{k}+\boldsymbol{q}} - \xi_{\boldsymbol{k},\sigma} - \xi_{\boldsymbol{q},\Gamma}}\right) F^{(m)}_{\sigma}(k_{\perp},k_z) \\ =& \frac{1}{8\pi^2}\sum_{\Gamma}\int q_{\perp}\,\mathrm{d}q_{\perp}\int \mathrm{d}q_z G^{(m)}_{\sigma,\Gamma}(k_{\perp},k_z;q_{\perp},q_z) F^{(m)}_{\Gamma}(q_{\perp},q_z), \end{aligned} \quad (16)$$

where we have defined the auxiliary function

$$\begin{aligned} &G^{(m)}_{\sigma,\Gamma}(k_{\perp},k_z;q_{\perp},q_z) \\ =& \frac{1}{\pi}\int_0^{2\pi} \mathrm{d}(\phi_{\boldsymbol{k}} - \phi_{\boldsymbol{q}}) \frac{\cos(m(\phi_{\boldsymbol{k}} - \phi_{\boldsymbol{q}})) R_{\boldsymbol{k},\sigma} L_{\boldsymbol{k},\sigma}}{E_3 - \varepsilon^{b}_{\boldsymbol{k}+\boldsymbol{q}} - \xi_{\boldsymbol{k},\sigma} - \xi_{\boldsymbol{q},\Gamma}}. \quad (17) \end{aligned}$$

3.1. Binding energy and wavefunction

We consider the system to be near a Feshbach resonance between atom b and the spin-up state of atom a, allowing the dimensionless interaction parameter $(\lambda a_s)^{-1}$ to be smoothly varied from the resonance point, where $(\lambda a_s)^{-1} = 0$, to the Bose–Einstein condensate (BEC) regime.

In Fig. 2, we show the variation of the trimer binding energy as a function of real and imaginary magnetic field strengths for a fixed mass ratio of $\eta = 40/6$ and interaction strength $(\lambda a_s)^{-1} = 0.5$. We find that in the case of a real magnetic field, as the field strength increases, the trimer binding energy E_{3b} rapidly decays to zero, indicating that the real magnetic field suppresses three-body pairing. In contrast, under the influence of an imaginary magnetic field, the behavior of the three-body binding energy is non-monotonic as the field strength increases. At the initial stage of increasing the field strength, the real part of the trimer binding energy $\mathrm{Re}(E_{3b})$ deepens gradually, and the dissipation of the trimer bound state $\mathrm{Im}(E_{3b})$ increases, remaining on the same order as the single-particle dissipation B. However, as the imaginary magnetic field strength continues to increase, the trimer binding weakens, and the imaginary part $\mathrm{Im}(E_{3b})$ begins to decrease as well. This is because when the field strength grows, the location of the minimum energy of the single-particle dispersion of particle a shifts from the Rashba ring to the point at zero momentum. As the imaginary magnetic field strength increases further, we observe that the changes in both the real and imaginary parts of the three-body binding energy become very slow, which is due to the quantum Zeno effect under strong dissipation.

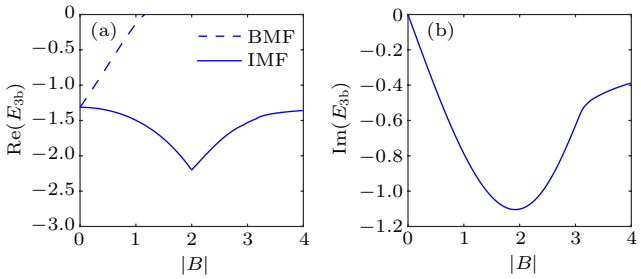


Fig. 2. The trimer binding energy E_{3b} as a function of the magnitude of the magnetic field strength. (a) The real part of binding energy decreases rapidly to zero as the strength of the real magnetic field (RMF) increases, while it exhibits a non-monotonic behavior as the strength of the imaginary magnetic field (IMF) increases. (b) The imaginary part of the three-body binding energy as a function of the IMF strength. The parameters used are mass ratio $\eta = 40/6$, interaction strength $(\lambda a_s)^{-1} = 0.5$, and the energy and Zeeman field strength are measured in units of $E_0 = \lambda^2/(2m_a)$.

To further investigate the system, we also analyze the variation of the trimer binding energy E_{3b} with other parameters. In Fig. 3, we show the variation of the trimer binding energy E_{3b} with the mass ratio η and the interaction strength $(\lambda a_s)^{-1}$ under the condition of an imaginary magnetic field $|B| = E_0$ and an interaction strength of $(\lambda a_s)^{-1} = 0.5$. We find that increasing the mass ratio η makes the real part of the trimer binding energy $\mathrm{Re}(E_{3b})$ deeper while rapidly suppressing the dissipation of the trimer bound state $\mathrm{Im}(E_{3b})$. In the limit of large η, we observe an extremely deep three-body binding energy $\mathrm{Re}(E_{3b})$, which is inconsistent with the case of no dissipation in previous study.[34] Additionally, we find that $\mathrm{Im}(E_{3b})$ approaches zero in the large η limit. The mechanism behind this phenomenon is that as the atom b becomes lighter, the corresponding kinetic energy dominates in the three-body scattering matrix and therefore suppresses the single-particle dissipation from SOC atom a.

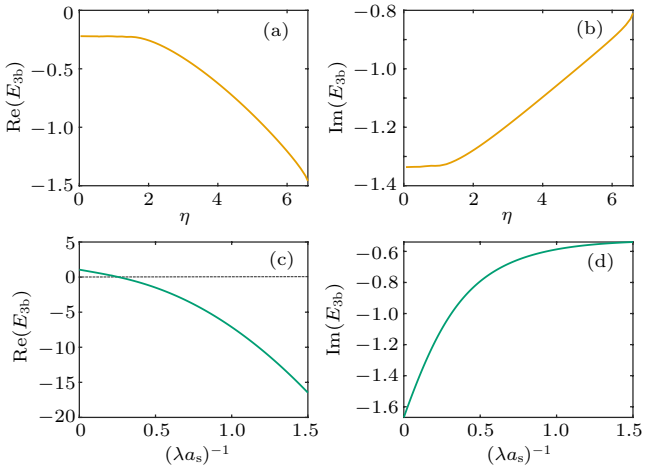


Fig. 3. The trimer binding energy E_{3b} as a function of the mass ratio η and interaction strength $(\lambda a_s)^{-1}$. (a) The real part of binding energy E_{3b} increases rapidly as the mass ratio η increases. (b) The imaginary part of the trimer binding energy E_{3b} decreases as the mass ratio η increases. In both (a) and (b), we fix the parameters as $B = \mathrm{i}$ and $(\lambda a_s)^{-1} = 0.5$. (c) The real part of the three-body binding energy E_{3b} as a function of the interaction strength $(\lambda a_s)^{-1}$. The three-body system forms a bound state at the three-body threshold $(\lambda a_s)^{-1} = 0.26$ and becomes more deeply bound as the interaction strength increases. (d) The imaginary part of the three-body binding energy E_{3b} decreases as the interaction strength $(\lambda a_s)^{-1}$ increases, remaining on the same order of magnitude as the single-particle dissipation $|B|$. The parameters in (c) and (d) are $B = \mathrm{i}$ and $\eta = 40/6$. The energy and Zeeman field strength are measured in units of $E_0 = \lambda^2/(2m_a)$.

We also show the variation of the trimer binding energy with the interaction strength $(\lambda a_s)^{-1}$ under the conditions of an imaginary magnetic field $|B| = E_0$ and a mass ratio of $\eta = 40/6$. As the interaction strength $(\lambda a_s)^{-1}$ increases, a trimer bound state forms at the interaction threshold $(\lambda a_s)^{-1} = 0.26$, and the binding becomes stronger as the interaction strength increases. It is worth noting that compared to the interaction threshold of $(\lambda a_s)^{-1} = 0.2$ in the absence of dissipation, a stronger interaction is required to form binding in the presence of dissipation. This behavior is in sharp contrast to previous study where dissipation promotes the formation of two-body binding.[29,37]

To further understand the role of the non-Hermicity in three-body pairing, we analyze the probability distribution of the wave function for the trimer bound state. As shown in

Figs. 4(a) and 4(e), we present the probability distribution $|\psi_{\mathrm{R}}^{(3)}(0;\boldsymbol{k},-;-\boldsymbol{k},-)|^2$ in the (k_x,k_y) plane for the parameters $(\lambda a_{\mathrm{s}})^{-1}=0.5,\eta=40/6$ under two conditions of $B/E_0=0.8\mathrm{i}$ and $B/E_0=4\mathrm{i}$. Similar to the probability distribution of the three-body wave function in the absence of dissipation in previous study, the distribution exhibits a double-peak pattern in the (k_x,k_y) plane, symmetric around the zero momentum point $\boldsymbol{k}=0$. However, in the presence of dissipation, the axial distribution of the wave function changes, and the peak of the probability distribution is no longer strictly concentrated around the Rashba ring.

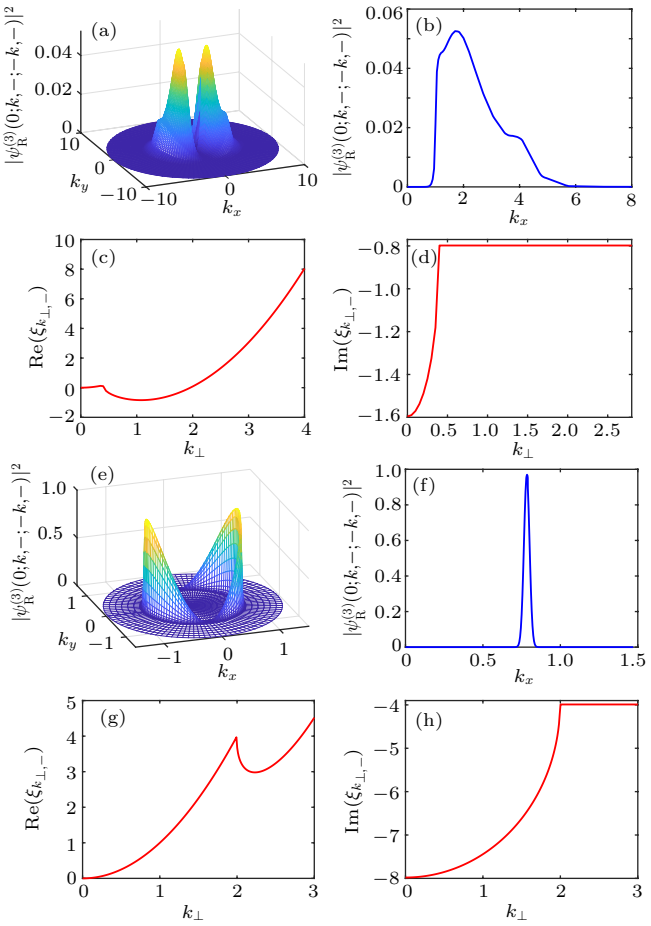


Fig. 4. The probability distribution of the three-body wave function $|\psi_{\mathrm{R}}^{(3)}(-\boldsymbol{k}-\boldsymbol{q};\boldsymbol{k}\sigma;\boldsymbol{q}\Gamma)|^2$ and the single-particle dispersion $\xi_{\boldsymbol{k},\pm}$. (a) The probability distribution of the three-body wave function $|\psi_{\mathrm{R}}^{(3)}(0;\boldsymbol{k},-;-\boldsymbol{k},-)|^2$ in the (k_x,k_y) plane at $k_z=0$. (b) The probability distribution of the three-body wave function $|\psi_{\mathrm{R}}^{(3)}(0;\boldsymbol{k},-;-\boldsymbol{k},-)|^2$ along the k_x axis at $k_y=0,k_z=0$. (c) The real part of the single-particle dispersion $\xi_{\boldsymbol{k},-}$ for particle a as a function of $k_\perp$ at $k_z=0$. (d) Another plot of the real part of the single-particle dispersion $\xi_{\boldsymbol{k},-}$ for particle a as a function of $k_\perp$ at $k_z=0$. The parameters used in (a)–(d) are $B=0.8\mathrm{i}$, $(\lambda a_{\mathrm{s}})^{-1}=0.5$, and $\eta=40/6$. (e) The probability distribution of the three-body wave function $|\psi_{\mathrm{R}}^{(3)}(0;\boldsymbol{k},-;-\boldsymbol{k},-)|^2$ in the (k_x,k_y) plane at $k_z=0$. (f) The probability distribution of the three-body wave function $|\psi_{\mathrm{R}}^{(3)}(0;\boldsymbol{k},-;-\boldsymbol{k},-)|^2$ along the k_x axis at $k_y=0,k_z=0$. (g) The real part of the single-particle dispersion $\xi_{\boldsymbol{k},-}$ for particle a as a function of $k_\perp$ at $k_z=0$. (h) Another plot of the real part of the single-particle dispersion $\xi_{\boldsymbol{k},-}$ for particle a as a function of $k_\perp$ at $k_z=0$. The parameters used in (e)–(h) are $B=4\mathrm{i}$, $(\lambda a_{\mathrm{s}})^{-1}=0.5$, and $\eta=40/6$. Energy and Zeeman field strength are measured in units of $E_0=\lambda^2/(2m_a)$, and momentum in units of λ.

To visualize the change in probability distribution more intuitively, we show in Figs. 4(b) and 4(f) the probability distribution $|\psi_{\mathrm{R}}^{(3)}(0;\boldsymbol{k},-;-\boldsymbol{k},-)|^2$ on the k_x axis by setting $k_y=0$ and $k_z=0$. It can be seen that in the case of small dissipation $|B|=0.8E_0$, the peak of the probability distribution is shifted toward higher momentum compared to the Rashba ring in Fig. 4(c), and the probability decays slowly as momentum k_x increases. From Fig. 4(d), we can see that the single-particle dissipation is not negligible in the region where the probability distribution is mainly concentrated, which explains the dissipation scale of the trimer state when the single-particle dissipation is small.

In the case of high dissipation $|B|=4E_0$, we find that the probability distribution $|\psi_{\mathrm{R}}^{(3)}(0;\boldsymbol{k},-;-\boldsymbol{k},-)|^2$ forms a highly localized peak along the k_x axis, as shown in Fig. 4(f). Compared to the single-particle dispersion in Figs. 4(g) and 4(h), we observe that the peak of the probability distribution $|\psi_{\mathrm{R}}^{(3)}(0;\boldsymbol{k},-;-\boldsymbol{k},-)|^2$ is located inside the EP and Rashba rings. This is related to the increase in the real part of the energy at the Rashba ring, where the minimum single-particle energy now occurs at the zero momentum, hindering the possibility of low-energy scattering and pairing around the Rashba ring. Consequently, the peak of the three-body probability distribution $|\psi_{\mathrm{R}}^{(3)}(0;\boldsymbol{k},-;-\boldsymbol{k},-)|^2$ shifts closer to zero momentum. Moreover, as the single-particle dissipation $|B|$ continues to increase, the real part of the energy at both the EP and Rashba rings continues to rise, and the peak of the three-body probability distribution $|\psi_{\mathrm{R}}^{(3)}(0;\boldsymbol{k},-;-\boldsymbol{k},-)|^2$ moves even closer to zero momentum, which is consistent with our analysis.

4. Phase diagram

It should be noted that in Fig. 2(a), we observe that the binding strength of the trimer state $\mathrm{Re}(E_{3\mathrm{b}})$ increases as the strength of the imaginary magnetic field increases. This indicates that the region where the trimer state can stably exist is modulated by the presence of single-body dissipation. To explore this further, we calculate the phase diagram of the system in the parameter space of magnetic field strength $|B|$ and interaction strength $(\lambda a_{\mathrm{s}})^{-1}$, with a fixed mass ratio of $\eta=40/6$, as shown in Fig. 5. We find that under real magnetic fields, the interaction thresholds for forming both dimer and trimer bound states decrease as the magnetic field strength increases, shifting the interaction strength threshold $(\lambda a_{\mathrm{s}})^{-1}$ toward the BEC side. Meanwhile, we observe that the interaction strength interval for both the Borromean phase $(\mathrm{Re}(E_{3\mathrm{b}})<0,\mathrm{Re}(E_{\mathrm{b}})=0)$ and the ordinary trimer phase $(\mathrm{Re}(E_{3\mathrm{b}})<\mathrm{Re}(E_{\mathrm{b}})<0)$ decreases. This suggests that the weakening effect of the real magnetic field on the two-body binding depth E_{b} is less than that on the three-body binding depth $E_{3\mathrm{b}}$, which explains why, under strong magnetic

fields, only the dimer phase ($\mathrm{Re}(E_\mathrm{b}) < \mathrm{Re}(E_{3\mathrm{b}}), \mathrm{Re}(E_\mathrm{b}) < 0$) and the scattering phase ($\mathrm{Re}(E_\mathrm{b}) > 0, \mathrm{Re}(E_{3\mathrm{b}}) > 0$) remain in the system.

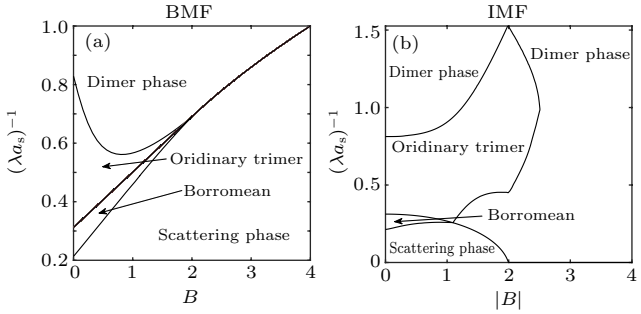


Fig. 5. The phase diagram of the system in the space of magnetic field strength and interaction strength. (a) The phase diagram of the system under the influence of a real magnetic field (RMF) shows that as the RMF strength increases, the interaction strength thresholds for both two-body and three-body binding are suppressed, while the interaction strength range for the existence of the ordinary trimer phase decreases rapidly. (b) The phase diagram of the system under the influence of an imaginary magnetic field (IMF) shows that the IMF suppresses the interaction strength threshold for three-body binding and enhances the threshold for two-body binding. Moreover, the IMF strengthens the three-body binding more significantly than the two-body binding at a fixed interaction strength $(\lambda a_\mathrm{s})^{-1}$, expanding the region where the ordinary trimer phase exists. The parameters used in the figure are $\eta = 40/6$, and the energy and Zeeman field strength are measured in units of $E_0 = \lambda^2/(2m_a)$.

In Fig. 5(b), we show the phase diagram of the system under an imaginary magnetic field. Consistent with previous discussions, the presence of an imaginary magnetic field facilitates the formation of dimer bound states, with the interaction threshold $(\lambda a_\mathrm{s})^{-1}$ for the two-body bound state shifting toward the resonance region as the magnetic field strength $|B|$ increases. At the same time, the imaginary magnetic field suppresses the formation of trimer bound states, with the interaction strength threshold $(\lambda a_\mathrm{s})^{-1}$ for the three-body bound state shifting toward the BEC side as the magnetic field strength increases, causing the Borromean phase of the system to rapidly vanish as the Zeeman field strength increases. We also observe that as the interaction strength increases to the BEC limit, the system exhibits only the dimer phase, with the trimer phase appearing only near the unitary region. This observation aligns with the physical picture in Hermitian systems. On the other hand, although the imaginary Zeeman field suppresses three-body binding, the trimer binding depth $\mathrm{Re}(E_{3\mathrm{b}})$ increases to some extent under a fixed interaction strength $(\lambda a_\mathrm{s})^{-1}$. In a certain range of imaginary magnetic field strengths, this increase in depth can be deeper than the two-body binding depth $\mathrm{Re}(E_\mathrm{b})$, resulting in an expansion of the region where the ordinary trimer phase exists within that range. Correspondingly, a phase boundary appears between the dimer phase and the ordinary trimer phase. We observe that with the addition of particle dissipation, the number of possible phases in the system changes, which also implies more experimental ways to control the system's states. Meanwhile, we point out that the variation of the phase boundary differs as IMF crosses $|B| = 2$, consistent with our analysis in Figs. 2 and 4, this behavior also arises from the change in the dispersion spectrum of atom a. As the Zeeman field strength crosses $|B| = 2$, the minimum of atom a's spectral dispersion shifts from the Rashba ring to zero momentum. The low-energy single-particle subspace plays a decisive role in determining the properties of the few-body states.

5. Summary and discussion

In conclusion, we have shown that a Borromean state and an enlarged trimer phase emerge in a three-body system under the Rashba SOC and an imaginary Zeeman field. The occurrence of Borromean state is attributed to the spectral symmetry in the single-particle dispersion of the spin–orbit coupled atom and the spin-selective inter-atomic interaction. The expansion of the trimer phase is due to the enhancement of the trimer binding energy by the imaginary magnetic field. The trimer state can be detected by measuring radio frequency spectrum of an atomic gas, a promising example is the ^{40}K–^{40}K–^{6}Li Fermi–Fermi mixtures. Our results highlight the interplay of interaction effect and non-Hermiticity in a few-body system. Our studies pave the way for further theoretical and experimental study of non-Hermitian physics in the few- and many-body systems. Future studies would include a further generation of the three-body pairing to the many-body physics.

Acknowledgements

We thank Wei Yi and Lihong Zhou for helpful discussions. This work has been supported by the National Natural Science Foundation of China (Grant No. 11974331).

References

[1] Daley A 2014 *Adv. Phys.* **63** 77
[2] Dalibard J, Castin Y and Mølmer K 1992 *Phys. Rev. Lett.* **68** 580
[3] Carmichael H J 1993 *Phys. Rev. Lett.* **70** 2273
[4] Ashida Y, Gong Z and Ueda M 2020 *Adv. Phys.* **69** 249
[5] El-Ganainy M, Makris K G, Khajavikhan M, Musslimani Z H, Rotter S and Christodoulides D N 2017 *Nat. Phys.* **14** 11
[6] Ozdemir S K, Rotter S, Nori F and Yang L 2019 *Nat. Mater.* **18** 783
[7] Miri M A and Alù A 2019 *Science* **363** 6422
[8] Chen W, Ozdemir S K, Zhao G, Wiersig J and Yang L 2017 *Nature* **548** 192
[9] Hodaei H, Hassan A U, Wittek S, Garcia-Gracia H, El-Ganainy R, Christodoulides D N and Khajavikhan M 2017 *Nature* **548** 187
[10] Xu H, Mason D, Jiang L and Harris J E 2016 *Nature* **537** 80
[11] Doppler J, Mailybaev A and Böhm J 2016 *Nature* **537** 76
[12] Hassan A U 2017 *Phys. Rev. A* **96** 052129
[13] Wu Y, Liu W, Geng J, Song X, Ye X, Duan C K, Rong K and Du J 2019 *Science* **364** 878
[14] Naghiloo M, Abbasi M, Joglekar Y N and Murch K W 2019 *Nat. Phys.* **15** 1232
[15] Lapp S, Ang'ong'a S, An F A and Gadway B 2019 *New J. Phys.* **21** 045006
[16] Chen T, Gou W, Xie D, Xiao T, Yi W, Jing J and Yan B 2021 *NPJ Quantum Inf.* **7** 78
[17] Liu W, Wu Y, Duan C K, Rong X and Du J 2021 *Phys. Rev. Lett.* **126** 170506
[18] Lin Q, Li T, Xiao L, Wang K, Yi W and Xue P 2022 *Phys. Rev. Lett.* **129** 113601

[19] Li J, Harter A K, Liu J, deMelo J, Joglekar Y N and Luo L 2019 *Nat. Commun.* **10** 855
[20] Ren Z, Liu D, Zhao E, He C, Pak K, Li J and Jo G 2022 *Nat. Phys.* **18** 385389
[21] Syassen N, Bauer D M, Lettner M, Volz T, Dietze D, Garcia-Ripoll J J, Cirac J I, Rempe G and Dürr S 2008 *Science* **320** 1329
[22] Tomita T, Nakajima S, Danshita I, Takasu Y and Takahashi Y 2017 *Sci. Adv.* **3** e1701513
[23] Tomita T, Nakajima S, Takasu Y and Takahashi Y 2019 *Phys. Rev. A* **99** 031601(R)
[24] Sponselee K, Freystatzky L, Abeln B, Diem M, Hundt B, Kochanke A, Ponath T, Santra B, Mathey L, Sengstock K and Becker C 2018 *Quantum Sci. Technol.* **4** 014002
[25] Diehl S, Rico E, Baranov M A and Zoller P 2011 *Nat. Phys.* **7** 971
[26] Macieszczak K, Guta M, Lesanovsky O and Garrahan J P 2016 *Phys. Rev. Lett.* **116** 240404
[27] Zhou L and Cui X 2019 *iScience* **14** 257
[28] Yamamoto K, Nakagawa M, Adachi K, Takasan K, Ueda M and Kawakami N 2019 *Phys. Rev. Lett.* **123** 123601
[29] Zhou L, Yi W and Cui X 2020 *Phys. Rev. A* **102** 043310
[30] Zhou Z and Yu Z 2019 *Phys. Rev. A* **99** 043412
[31] Pan L, Chen S and Cui X 2019 *Phys. Rev. A* **99** 063616
[32] Ding P and Yi W 2022 *Chin. Phys. B* **31** 010309
[33] Vyasanakere J P, Zhang S and Shenoy V B 2011 *Phys. Rev. B* **84** 014512
[34] Cui X and Yi W 2014 *Phys. Rev. X* **4** 031026
[35] Qiu X, Cui X and Yi W 2016 *Phys. Rev. A* **94** 051604(R)
[36] Barontini G, Labouvie R, Stubenrauch F, Vogler A, Guarrera V and Ott H 2013 *Phys. Rev. Lett.* **110** 035302
[37] Zhao X and Zhou L 2023 *Phys. Rev. A* **108** 013311
[38] Sun M, Liu C and Shi Z 2023 *Phys. Rev. Res.* **5** 043010